TDDFT study of time-dependent and static screening in graphene

V. Despoja,[1,2,*] D. J. Mowbray,[3,2] D. Vlahović,[1] and L. Marušić[4]

[1]*Department of Physics, University of Zagreb, Bijenička 32, HR-10000 Zagreb, Croatia*
[2]*Donostia International Physics Center (DIPC), Paseo de Manuel de Lardizabal 4, ES-20018 San Sebastían, Spain*
[3]*Nano-Bio Spectroscopy Group and ETSF Scientific Development Center, Departamento de Física de Materiales,*
Universidad del País Vasco UPV/EHU, ES-20018 San Sebastían, Spain
[4]*Maritime Department, University of Zadar, M. Pavlinovića b.b., HR-23000 Zadar, Croatia*

Time-dependent density functional theory (TDDFT) within the random phase approximation (RPA) is used to obtain the time evolution of the induced potential produce by the sudden formation of a C 1s core hole inside a graphene monolayer, and to show how the system reaches the equilibrium potential. The characteristic oscillations in the time-dependent screening potential are related to the excitations of π and $\sigma + \pi$ plasmons as well as the low energy 2D plasmons in doped graphene. The equilibrium RPA screened potential is compared with the DFT effective potential, yielding good qualitative agreement. The self energy of a point charge near a graphene monolayer is shown to demonstrate an image potential type behavior, $Ze/(z - z_0)$, down to very short distances (4 a.u.) above the graphene layer. Both results are found to agree near quantitatively with the DFT ground state energy shift of a Li$^+$ ion placed near a graphene monolayer.

PACS number(s): 73.22.Pr, 73.22.Lp

I. INTRODUCTION

Graphene is a very simple, strong, and easily synthesized material,[1–6] which makes it interesting for many practical applications,[7–10] culminating in the award of a Nobel prize in 2011.[11,12] For example, bilayer and monolayer graphene on substrates[13] have become promising materials for both nanoelectronics[14] and optoelectronics.[15] Plasmon resonances in graphene produce enhanced near field effects similar to those in noble metals. However, graphene's simpler electronic structure makes it superior to the noble metals for photonics,[16] plasmonics,[17,18] nanosensing,[19] and heat transfer processes.[20]

For applications such as photonics and plasmonics, a better understanding is needed of the plasmon-photon switching mechanism[21] and plasmon-polariton decaying mechanisms. These strongly affect the life time and propagation length of plasmons-polaritons, such as electron-hole pairs and phonons.[17] Also, in many applications it is very important to understand how an external longitudinal probe, e.g., an external charge distribution, should be designed in order to both efficiently and selectively excite plasmons in graphene. Even though there are many theoretical[22–24] and experimental[25–27] investigations of plasmonics and single particle excitations in graphene, a proper theoretical description of the plasmon excitation and decay mechanisms is still lacking.

In this paper we investigate the time scale at which a simple longitudinal probe excites various plasmons in pristine and doped graphene. In particular, we focus on the time evolution of the induced potential produced by a suddenly created point charge inside a graphene monolayer ($z = 0$). This is a realistic model for the creation of a 1s core hole in a carbon atom in graphene, i.e., a C1s core hole. Such information may prove quite important for describing the core-hole screening in x-ray adsorption and photoemission spectroscopy experiments. We show that the short time scale features ($t < 2$ fs) in the induced potential are due to excitations of high energy π and $\sigma + \pi$ plasmons. On the other hand, the long time scale ($2 < t < 15$ fs) oscillations of the induced potential are only present

when graphene is doped, and are due to the excitation of low energy 2D plasmons.

To calculate the induced potential we use the response function obtained from first principles time-dependent density functional theory (TDDFT) within the random phase approximation (RPA). This allows us to include contributions from all electronic excitations up to 25 eV, while neglecting crystal local field effects (LFEs) parallel to the graphene surface. We also compare equilibrium values ($t \to \infty$) for the TDDFT-RPA screened potential with the ground state density functional theory (DFT) effective potential calculated using a much larger supercell with a C1s core hole. This allows us to determine under which conditions LFEs parallel to the surface may be neglected when describing the screened potential.

We also calculate the RPA self energy or polarization shift for a static point charge as a function of its height z above the graphene monolayer. The RPA self energy is found to display an image potential behavior $Ze/(z - z_0)$ down to very short distances ($z \approx 4$ a.u.) above pristine or doped graphene monolayers. Our results are in good agreement with recent DFT ground state calculations of graphene in external electrical fields,[28] which found the centroid of the induced charge density at $z_0 \approx 1.97$ a.u. These results are further compared with a DFT calculation of a Li$^+$ ion's self energy as a function of the ion's height above a graphene monolayer.

This paper is organized as follows. In Sec. II we describe the first principles methods used to calculate the ground state Kohn-Sham orbitals in graphene, the RPA response and dielectric matrices, and the propagator of the dynamical Coulomb interaction. From this we derive an expression for the time-dependent induced potential near a graphene monolayer. In Sec. III we discuss our results. We first consider in Sec. III A the time evolution of the induced potential produced by a point charge suddenly created inside a graphene monolayer. The spatial dependence of the induced potential at equilibrium is then compared in Sec. III B with a ground state DFT calculation of the change in effective potential due to a C1s

core hole. Finally, in Sec. III C the RPA self energy for a point charge is then compared with the DFT self energy for a Li$^+$ ion as a function of height z above a graphene monolayer. This is followed by concluding remarks in Sec. IV.

II. METHODOLOGY

We shall begin by briefly describing the computational methods used to calculate the Kohn-Sham wave functions and energy levels, i.e., band structure, of a graphene monolayer. These results will later be used to calculate the free electron response function and induced effective potentials.

Although the unit cell employed to calculate the ground state wave functions is periodic normal to the graphene layers, this periodicity is removed when calculating the response function. This is accomplished by an appropriate choice of boundaries for integration normal to the graphene layers, allowing us to describe an isolated graphene monolayer.

We use the experimental unit cell parameter of $a \approx 4.651$ a.u., with the graphene layers separated by $L = 5a \approx 23.255$ a.u. Electronic structure calculations for graphene are performed using two different *ab initio* DFT codes. We use both the plane-wave self-consistent field code PWscf belonging to the Quantum Espresso (QE) package[29] and the real space projector augmented wave function (PAW) code GPAW.[30,31] In both cases we employ the Perdew-Zunger local density approximation (LDA) for the exchange correlation (xc) potential.[32] Here, the xc functional is approximated by the functional derivative of the exchange and correlation potential of a homogeneous electron gas.[33] An electronic temperature of $k_B T \approx 0.1$ eV is used to achieve convergence of the Kohn-Sham wave functions, with all energies extrapolated to 0 K. The electronic density is calculated using a $12 \times 12 \times 1$ Γ-centered Monkhorst-Pack special k-point mesh,[34] i.e., we use 19 special points in the irreducible Brillouin zone (BZ), as shown in Fig. 1(a).

In PWscf we use norm-conserving LDA based pseudopotentials for carbon.[35] We find the energy spectrum is converged for a 50 Ry plane-wave cutoff. For GPAW we use a grid spacing of $h \approx 0.2$ Å. The graphene band structure along the high symmetry K $\rightarrow$ Γ $\rightarrow$ M $\rightarrow$ M$'$ $\rightarrow$ K directions shown in Fig. 1(b) is calculated along a path with 176 k points. Here we have used the overlaps between the Kohn-Sham wave functions at successive k points $\langle \Phi_{n,\mathbf{k}} | \Phi_{n',\mathbf{k}+\triangle\mathbf{k}} \rangle$ to differentiate between band crossings and avoided crossings, as described in Ref. 36.

DFT calculations of the induced potential due to a C1s core hole have been performed within GPAW. This is accomplished by taking the difference in the effective potential for graphene with and without employing a pseudopotential with a full core hole in the 1s level for one of the carbon atoms. We have used a supercell consisting of $9 \times 9 \times 1$ repeated graphene unit cells, to ensure interactions between periodic core-hole images may be neglected. For such a large unit cell, we find a Γ point calculation is sufficient to converge the electronic density, as seen from Fig. 1(a).

The self energy Σ of a static Li$^+$ ion in the vicinity of a graphene layer is simply the difference in total energy between combined and separated Li$^+$ and graphene. The Li$^+$ ion is modeled by performing calculations with a charge of
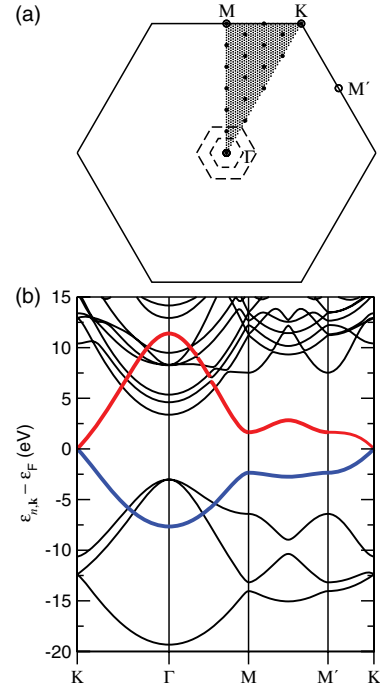

FIG. 1. (Color online) (a) Graphene Brillouin zone for primitive (solid lines), $5 \times 5 \times 1$ (long dashed lines), and $9 \times 9 \times 1$ (short dashed lines) repeated unit cells showing critical points (open circles) and Monkhorst-Pack k-point samplings employed for calculating the electron density (filled circles) and the density-density response function (points). (b) Graphene band structure $\varepsilon_{n,\mathbf{k}}$ in eV relative to the Fermi energy ε_F. Thick lines are the occupied π (blue) and unoccupied π^* (red) bands.

$Q = +1 e$, within a supercell of $5 \times 5 \times 1$ repeated graphene unit cells. In this case a $21 \times 21 \times 1$ Monkhorst-Pack k-point mesh has been used. From a Bader analysis of the all-electron charge density, we find in the combined Li$^+$-graphene system, a charge of $Q \gtrsim 0.9 e$ is localized on the Li atom for heights 1.5 Å $< z <$ 6 Å above graphene.

Using the ground state Kohn-Sham wave functions as input, we have implemented the following methodology for calculating the 2D density-density response function within TDDFT-RPA. The matrix of the noninteracting density-density response function χ^0 for a quasi-2D system may be expressed as

$$\chi^0_{\mathbf{G}_\parallel \mathbf{G}'_\parallel}(\mathbf{Q},\omega,z,z') = \frac{2}{S} \sum_{\mathbf{K}} \sum_{n,m} \frac{f_n(\mathbf{K}) - f_m(\mathbf{K}+\mathbf{Q})}{\omega + i\eta + \varepsilon_n(\mathbf{K}) - \varepsilon_m(\mathbf{K}+\mathbf{Q})}$$
$$\times M_{n\mathbf{K},m\mathbf{K}+\mathbf{Q}}(\mathbf{G}_\parallel,z) \, M^*_{n\mathbf{K},m\mathbf{K}+\mathbf{Q}}(\mathbf{G}'_\parallel,z').$$

(1)

Here S is the surface area of the unit cell, η is the peak broadening, and $f_n(\mathbf{K})$ and $\varepsilon_n(\mathbf{K})$ are the Fermi-Dirac occupation and energy, respectively, of the nth band at $\mathbf{K}$. The summation over $\mathbf{K}$ runs through 10303 Monkhorst-Pack special k points in the BZ or 901 in the irreducible BZ, as shown in Fig. 1(a). The n,m summation is performed over 50 bands, which is sufficient for a proper description of the high energy $\sigma + \pi$ plasmon in graphene. The matrix elements M have the form

$$M_{n\mathbf{K},m\mathbf{K}+\mathbf{Q}}(\mathbf{G}_\parallel,z) = \langle \Phi_{n\mathbf{K}} | e^{-i(\mathbf{Q}+\mathbf{G}_\parallel)\rho} | \Phi_{n\mathbf{K}+\mathbf{Q}} \rangle_S, \quad (2)$$

where $\mathbf{Q}$ and $\mathbf{G}_\parallel$ are the momentum transfer and reciprocal lattice vectors, respectively, in the (x,y) plane of the graphene surface. The integration is performed over the unit cell surface S, and the plane wave expansion of the Kohn-Sham wave functions is

$$\Phi_{n\mathbf{K}}(\boldsymbol{\rho},z) = \frac{1}{\sqrt{V}}e^{i\mathbf{K}\boldsymbol{\rho}} \sum_{\mathbf{G}} C_{n\mathbf{K}}(\mathbf{G})e^{i\mathbf{G}\mathbf{r}}, \qquad (3)$$

where $V = S \times L$ is the unit cell volume, $\mathbf{G} = (\mathbf{G}_\parallel, G_z)$ is a 3D reciprocal lattice vector, $\mathbf{r} = (\boldsymbol{\rho},z)$ is a 3D position vector with z normal to the surface, and the coefficients $C_{n\mathbf{K}}$ are obtained by solving the Kohn-Sham equations. Integration over the perpendicular z coordinate in expression (2) is not yet performed, so the matrix elements remain z dependent. The screened response function may be obtained from Eq. (1) by solving the combined integral-matrix equation

$$\chi_{\mathbf{G}_\parallel \mathbf{G}'_\parallel}(z,z') = \chi^0_{\mathbf{G}_\parallel \mathbf{G}'_\parallel}(z,z') + \sum_{\mathbf{G}_{\parallel 1}, \mathbf{G}_{\parallel 2}} \iint_{-\frac{L}{2}}^{\frac{L}{2}} dz_1 dz_2 \chi^0_{\mathbf{G}_\parallel \mathbf{G}_{\parallel 1}}(z,z_1)$$
$$\times\, V_{\mathbf{G}_{\parallel 1}\mathbf{G}_{\parallel 2}}(z_1,z_2)\chi_{\mathbf{G}_{\parallel 2}\mathbf{G}'_\parallel}(z_2,z'),$$

where we have suppressed the $\mathbf{Q}$ and ω dependence to simplify the expression. Note that the z_1 and z_2 integrations from $-\frac{L}{2}$ to $\frac{L}{2}$ ensure interactions between repeated images are removed. In this way we obtain a correct description for an isolated graphene monolayer. Here

$$V_{\mathbf{G}_\parallel \mathbf{G}_\parallel '}(z,z') = \delta_{\mathbf{G}_\parallel \mathbf{G}_\parallel '} V(\mathbf{Q} + \mathbf{G}_\parallel, z,z')$$
$$V(\mathbf{Q} + \mathbf{G}_\parallel, z,z') = \frac{2\pi}{|\mathbf{Q} + \mathbf{G}_\parallel|} e^{-|\mathbf{Q}+\mathbf{G}_\parallel||z-z'|} \qquad (4)$$

is the matrix of the bare Coulomb potential. After applying a Fourier transform in the z direction

$$f(G_z) = \frac{1}{\sqrt{L}} \int_{-\frac{L}{2}}^{\frac{L}{2}} dz e^{iG_z z} f(z); \quad G_z = \frac{2\pi\, n}{L}; \quad n \in \mathbb{Z}, \qquad (5)$$

Eq. (4) becomes a pure matrix equation. The solution of this equation, i.e., the matrix $\chi_{\mathbf{G}_\parallel \mathbf{G}'_\parallel}(G_z, G'_z)$, may then be inserted in the equation for the propagator of the induced Coulomb interaction

$$W^{\text{ind}}(\mathbf{Q} + \mathbf{G}_\parallel, \mathbf{Q}, \omega, z, z')$$
$$= \sum_{G_{z_1}, G_{z_2}} V(\mathbf{Q} + \mathbf{G}_\parallel, z, G_{z_1})\chi_{\mathbf{G}_\parallel}$$
$$\times (\mathbf{Q} + \mathbf{G}_\parallel, \omega, G_{z_1}, G_{z_2})V(\mathbf{Q}, G_{z_2}, z'). \qquad (6)$$

From hereon, we shall restrict consideration to the induced potential at positions $z > a$. According to Eq. (4), this means that the dominant contributions in Eq. (6) are the Fourier components $|\mathbf{Q} + \mathbf{G}_\parallel| < \frac{1}{a}$. From this we find that the $\mathbf{G}_\parallel \neq 0$ Fourier components are negligible. In other words, we only need to include the $\mathbf{G}_\parallel = 0$ components in Eq. (6). This means that for the systems considered herein, LFEs in the graphene plane may be neglected. Using Eqs. (4), (5), and (6), we may express the induced potential at z as

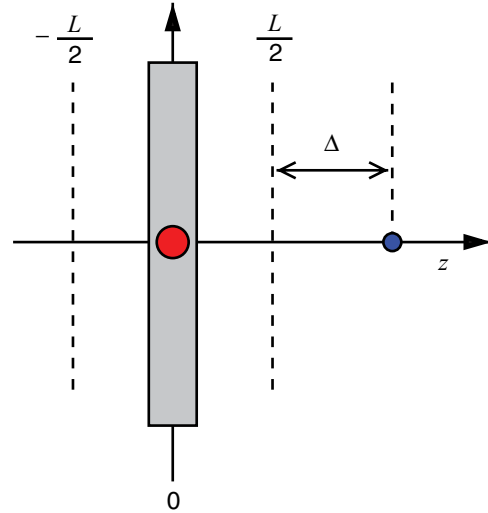$$W^{\text{ind}}(\mathbf{Q}, \omega, z, z' = 0) = e^{-Q\Delta} D(\mathbf{Q}, \omega), \qquad (7)$$

FIG. 2. (Color online) Schematic of a graphene layer showing the core-hole (larger red dot) and negative probe charge (smaller blue dot) positions. Unit cell parameter are $a = 4.651$ a.u. in the plane, and $L = 5a$ normal to the layer.

where $\Delta \equiv z - \frac{L}{2}$, as depicted schematically in Fig. 2. The function D is defined as

$$D(\mathbf{Q}, \omega) \equiv \sum_{G_z, G'_z} I(G_z)\chi(\mathbf{Q}, \omega, G_z, G'_z)J(G'_z), \qquad (8)$$

where

$$I(G_z) = (-1)^n \frac{2\pi}{\sqrt{L}Q} \frac{1 - e^{-QL}}{Q + iG_z}, \qquad (9)$$

$$J(G'_z) = \frac{4\pi}{\sqrt{L}} \frac{1 - (-1)^{n'} e^{-\frac{QL}{2}}}{Q^2 + G'^2_z}, \qquad (10)$$

with $G_z = \frac{2\pi n}{L}, n \in \mathbb{Z}$.

The function D has an explicit physical meaning. It is the $\mathbf{Q}$ component of the induced Coulomb potential at $z = \frac{L}{2}$ produced by a "flashing" point charge placed at $z' = 0$ (inside the graphene layer) with flashing frequency ω. To calculate the matrix $\chi(G_z, G'_z)$ we use an energy cutoff of 40 Ry, which corresponds to a 47×47 matrix. This cutoff is sufficient to provide a smooth, monotonically decaying tail for the induced charge density when $z > a$.

Another important assumption is that $D(\mathbf{Q}, \omega)$ is an isotropic function of $\mathbf{Q}$. This means that the intensity and frequency of the electronic modes should not depend on the propagation direction. However, this is not entirely true for realistic crystal structures. For example, the π plasmon dispersion in graphene and carbon nanotubes splits if $\mathbf{Q}$ is in the $\Gamma \rightarrow M$ direction but does not split if it is in the $\Gamma \rightarrow K$ direction.[37–39] This means we should average $\mathbf{Q}$ over the high symmetry directions.

To do so, we first calculate $D(\mathbf{Q}, \omega)$ for a particular point in the $\Gamma - M$ direction, and then for the corresponding point in the $\Gamma \rightarrow K$ direction for which $|\mathbf{Q}_{\Gamma \rightarrow K}| = |\mathbf{Q}_{\Gamma \rightarrow M}| = Q$. The average value of $D(\mathbf{Q}, \omega)$ is then

$$\overline{D}(Q, \omega) = \frac{D(\mathbf{Q}_{\Gamma M}, \omega) + D(\mathbf{Q}_{\Gamma K}, \omega)}{2}. \qquad (11)$$

The propagator of the induced potential at z then also becomes an isotropic function of $\mathbf{Q}$:

$$W^{\text{ind}}(Q,\omega,z,z'=0) = e^{-Q\Delta}\overline{D}(Q,\omega). \quad (12)$$

If we neglect the $\mathbf{G}_{\parallel} \neq 0$ components of W^{ind}, it becomes a translationally invariant function, i.e., a function of $\boldsymbol{\rho} - \boldsymbol{\rho}'$. In this case, the $(\mathbf{Q},\omega)$ Fourier transform of the induced potential can be calculated from

$$V^{\text{ind}}(Q,\omega,z) = \int_{-\infty}^{\infty} dz_1 W^{\text{ind}}(Q,\omega,z,z_1)\varrho^{\text{ext}}(Q,\omega,z_1), \quad (13)$$

where we assume the external charge distribution ϱ^{ext} is an isotropic function of $\boldsymbol{\rho}$. Since we are interested in the potential induced by a suddenly created C1s core hole at the origin, its charge distribution may be modeled using

$$\varrho^{\text{ext}}(\rho,z,t) = \delta(\rho)\delta(z)\Theta(t), \quad (14)$$

where $\Theta(t)$ is the Heaviside step function. After Fourier transforming Eq. (14) into (Q,ω) space, inserting it into Eq. (13) and integrating over z_1, the induced potential becomes

$$V^{\text{ind}}(Q,\omega,z) = W^{\text{ind}}(Q,\omega,z,0)\Theta(\omega), \quad (15)$$

where $\Theta(\omega)$ is the Fourier transform of Heaviside step function

$$\Theta(\omega) = \frac{i}{\omega} - \pi\delta(\omega). \quad (16)$$

Finally, after Fourier transforming back into real space and time, the induced potential is

$$V^{\text{ind}}(\rho,z,t) = \int_{-\infty}^{\infty} \frac{d\omega}{2\pi} e^{-i\omega t} \iint \frac{d\mathbf{Q}}{(2\pi)^2} e^{i\mathbf{Q}\cdot\boldsymbol{\rho}} V^{\text{ind}}(Q,\omega,z). \quad (17)$$

Rewriting in terms of D, from Eqs. (7) and (11) we find

$$\begin{aligned} &V^{\text{ind}}(\rho,z,t) \\ &= -\frac{1}{2\pi^2} \int_0^{Q_C} dQ\,Q\, e^{-Q\Delta} J_0(Q\rho) \\ &\quad \times \int_0^{\infty} \frac{d\omega}{\omega} \Im[\overline{D}(Q,\omega) e^{-i\omega t}] - \frac{1}{2} W^{\text{ind}}(\rho,\omega=0,z,0), \end{aligned} \quad (18)$$

where J_0 is the zeroth order Bessel function of the first kind.

From the definitions of the D function in Eqs. (6)–(8), it is easy to show that it behaves as $D \sim e^{-QL/2}$. This means that the integrand of the Q integration behaves as $\sim e^{-Qz}$. We may use this to define the cutoff wave vector Q_C. For positions $z \geqslant a$, i.e., those investigated here, $Q_C \leqslant \frac{1}{a} \approx 0.22$ a.u. However, we have chosen Q_C to be almost four times larger, namely $Q_C = 0.8$ a.u.

For such smooth Q dependent functions, integration is performed using the Gauss-Legendre method over 51 points. On the other hand, the ω integration is performed using a simple trapezoidal method with 2001 points up to 50 eV. In this way we ensure the inclusion of the entire spectral weight of the high energy $\sigma + \pi$ plasmon. The second term in Eq. (18) represents the induced potential in the adiabatic limit or equilibrium potential $V^{\text{ind}}(\rho,z,t \to \infty)$. We shall use expression (18) to calculate the time evolution of the induced potential at (ρ,z).

We also want to describe how the polarization energy or self energy of a charged particle depends on its height z above the graphene monolayer. The self energy of the static particle can be calculated using the function D defined by Eq. (8). However, the second form factor needs to be modified to reflect the fact that now both z and z' are outside the graphene monolayer, i.e.,

$$J(G_z') \to I^*(G_z'). \quad (19)$$

After this modification the D function becomes

$$D \to \widetilde{D}(Q,\omega) = \frac{Q}{2\pi} \sum_{G_z,G_z'} I(G_z)\chi(Q,\omega,G_z,G_z')I^*(G_z'). \quad (20)$$

The quantity $\widetilde{D}$ represents the (Q,ω) component of the induced potential at $z = L/2$ caused by a flashing point charge placed at $z' = L/2$. The static point charge self energy at point z can then be calculated using[40]

$$\Sigma(z) = \frac{1}{2} \int_0^{Q_c} dQ\, e^{-2Q\Delta} \widetilde{D}(Q,\omega=0), \quad (21)$$

where the cutoff wave vector $Q_c = 0.8$ a.u., as defined above.

For larger distances $\Delta \geqslant 0$ only $Q \approx 0$ components contribute. Expanding $\widetilde{D}(Q,\omega)$ to linear order in Q,

$$\widetilde{D}(Q,\omega=0) \approx Z + \alpha Q, \quad (22)$$

where

$$Z = \widetilde{D}(Q=0,\omega=0), \quad (23)$$

$$\alpha = \frac{d\widetilde{D}(Q=0,\omega=0)}{dQ}. \quad (24)$$

After inserting Eq. (22) into Eq. (21), the integral over Q may be calculated analytically, yielding

$$\Sigma(z) \approx -\frac{Z}{4(z-z_0)}. \quad (25)$$

From this we see that Z is an effective image charge and

$$z_0 \approx \frac{L}{2} + \frac{\alpha}{2Z} \quad (26)$$

is the effective image plane measured from the center of the graphene layer, i.e., from $z = 0$.

III. RESULTS AND DISCUSSION

A. Time-Dependent Response

Let us now examine how the features appearing in the time evolution of the induced potential are related to the characteristic excitations in graphene. Each ω component of a suddenly created point charge excites all Q modes simultaneously. For this reason, the frequency of oscillations in the induced potential should be compared with the frequencies at which the integrated spectral function, defined as

$$\alpha(\omega) = -\frac{1}{\omega} \int_0^{\infty} \frac{Q\,dQ}{2\pi^2} \Im[\overline{D}(Q,\omega)], \quad (27)$$

has maxima.

This expression resembles the dynamical singularity index used to calculate the core hole spectral function.[40] However,
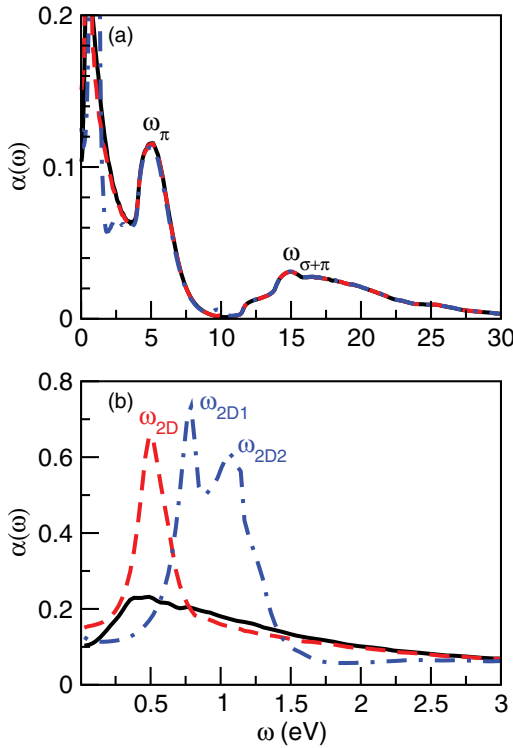
FIG. 3. (Color online) Nonlocal singularity index $\alpha(\omega)$ vs plasmon energy ω in eV for graphene with dopings of $\varepsilon_F = 0$ (black solid line), $\varepsilon_F = 0.5$ eV (red dashed line), and $\varepsilon_F = 1$ eV (blue dash-dotted line). (a) Broad peaks corresponding to the π and $\sigma + \pi$ plasmons. (b) Sharp peaks (with positions increasing with doping) corresponding to 2D or Drude plasmons.

an important difference is that α is calculated from the induced potential obtained at different points, $z = 0$ and $z' = \frac{L}{2}$. For this reason we shall refer to α as a nonlocal singularity index.

Figure 3 shows the nonlocal singularity index for pristine and doped graphene at high and low energy scales. In Fig. 3(a) we see two broad peaks, at 5 and 15 eV, which correspond to π and $\sigma + \pi$ plasmons, respectively. In Fig. 3(b) we see plasmon peaks which shift to higher energy as doping is increased. These peaks correspond to 2D or Drude plasmons which result from extra electronic plasma in the partially filled π^* band, shown in Fig. 1(b).[22] The broad peak for pristine graphene comes from the continuum of $\pi \rightarrow \pi^*$ interband transitions.

We shall next examine how the period of oscillations in the induced potential (18) correspond to the frequencies at which the peaks in the nonlocal singularity index α appear. To achieve this, it is useful to introduce an expression which connects the period of oscillations appearing in (18) in fs with the frequency of the peak positions in Fig. 3 in eV,

$$T \text{ [fs]} = \frac{4.1357}{\omega \text{ [eV]}}. \quad (28)$$

It is clear that the short time scale features in the induced potential of Eq. (18) correspond to high energy peaks shown in Fig. 3, while the long time scale features in the induced potential correspond to small energy peaks shown in Fig. 3(b).

Figure 4 shows the time evolution of the induced potential at $z = 1.5a \approx 7$ a.u. in the first 2 fs after the formation of a core hole at $z = 0$. We find the screening potential does
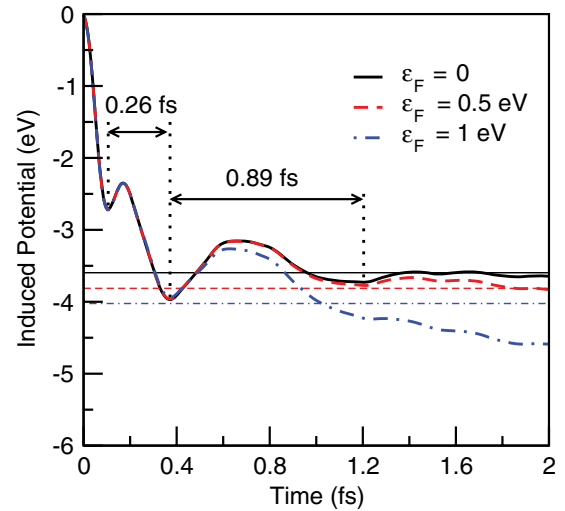

FIG. 4. (Color online) Time evolution in fs of the induced potential in eV at $z = 7$ a.u., $\rho = 0$ due to a core hole at the origin formed at $t = 0$, for undoped graphene (black solid line), $\varepsilon_F = 0.5$ eV (red dashed line), and $\varepsilon_F = 1$ eV (blue dash-dotted line). The corresponding equilibrium (static) values are marked by thin horizontal lines.

not approach the equilibrium (static) value monotonically, but instead exhibits some damped oscillations. Obviously there are some restoring mechanisms which force the system to oscillate before reaching equilibrium.

From Fig. 3(a), we see that the frequency at which the $\sigma + \pi$ plasmon causes a maximum in α is around $\omega_{\sigma + \pi} \approx 15$ eV, while the π plasmon frequency is $\omega_\pi \approx 5$ eV. According to expression (28), these frequencies correspond with periods $T_{\sigma + \pi} \approx 0.28$ fs and $T_\pi \approx 0.83$ fs. On the other hand, the period of the first oscillation in Fig. 4 is 0.26 fs and the frequency of the second oscillation is 0.89 fs. This suggests that these oscillations correspond to $\sigma + \pi$ and π plasmons, respectively.

We also find that for times shorter than 1 fs, doping has almost no influence on the dynamics of the induced potential. This is because doping introduces an excess 2D plasma, and the corresponding low energy plasmons can only influence the dynamics at longer time scales.

We next consider the behavior of the induced potential more than 2 fs after the core hole is formed. From Fig. 5 we see that the induced potential in pristine graphene has already achieved static values after 2 fs, while for doped graphene it continues to oscillate. The average period of these oscillations for $\varepsilon_F = 0.5$ eV is $\overline{T}_{2D(0.5eV)} \approx 8.6$ fs. The corresponding α shown in Fig. 3(b) has a sharp peak at around $\omega_{2D} \approx 0.5$ eV which, from Eq. (28), gives $T_{2D(0.5eV)} \approx 8.3$ fs. This suggests that these oscillations are attributable to excitations of doping induced 2D plasmons.

We also find that the plasma continues to oscillate with the same period and does not reach equilibrium even after 15 fs. For $\varepsilon_F = 1$ eV, the situation is slightly different. Namely, the singularity index shown in Fig. 3(b) has two peaks, in contrast to the single peak for $\varepsilon_F = 0.5$ eV. One peak is at $\omega_{2D1} \approx 0.8$ eV, while the other is at $\omega_{2D2} \approx 1.1$ eV.

This results in the occurrence of features in the induced potential which are characteristic of a superposition of two
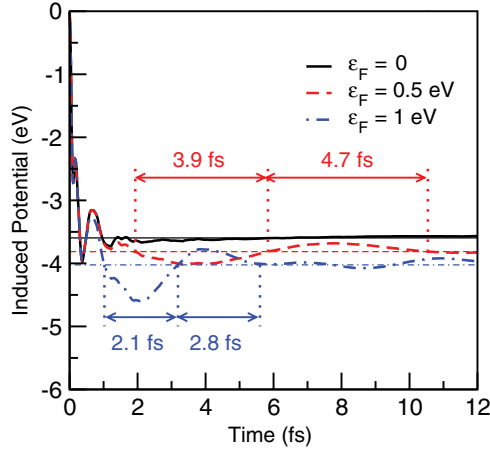
FIG. 5. (Color online) Time evolution in fs of the induced potential in eV at $z = 7$ a.u., $\rho = 0$ due to a core hole at the origin formed at $t = 0$, for undoped graphene (black solid line), $\varepsilon_F = 0.5$ eV (red dashed line), and $\varepsilon_F = 1$ eV (blue dash-dotted line). The corresponding equilibrium (static) values are marked by thin horizontal lines.

modes with similar frequencies. Specifically, we find fast oscillations at an average frequency with slow variations in amplitude known as beats. The period of the fast oscillations obtained from two semi-periods shown in Fig. 5 is $T_{2D(1eV)} \approx$ 4.9 fs. The average frequency of the two peaks shown in Fig. 3(b) is

$$\omega_{av} = \frac{\omega_{2D1} + \omega_{2D2}}{2} \approx 0.95 \text{ eV}, \qquad (29)$$

which from Eq. (28) gives $T_{av} \approx 4.4$ fs. At $t \approx 7$ fs, the induced potential approaches its equilibrium value, but the amplitude again increases and reaches another maximum at $t \approx 14$ fs. From the peak frequencies in Fig. 3(b), the beats frequency is

$$\omega_b = \omega_{2D1} - \omega_{2D2} \approx 0.28 \text{ eV}, \qquad (30)$$

which combined with Eq. (28) gives $T_b \approx 15$ fs. There is good agreement between T_{av} and T_b obtained from the peak frequencies in Fig. 3(b) and the period of fast and slow oscillations in Fig. 5.

The reason why α has two peaks instead of one peak still remains unclear. Inspection of each Q component contributing to α shows that only the long wavelength components ($Q \leqslant$ 0.015 a.u.) have two peaks. To ensure that these peaks are not numerical artifacts we also plotted the real part of each long wavelength component of $\overline{D}(Q,\omega)$. We found that at the position of each peak of $\Im[\overline{D}(Q,\omega)]$, $\Re[\overline{D}(Q,\omega)]$ has either a dip or a zero. Moreover, by inspecting the frequencies of the single particle excitations, from $-\Im[\chi_0(Q,\omega)]$, we found two split maxima. One of these is strong while the other one is very weak, with frequencies related to ω_{2D1} and ω_{2D2}. It seems that in the long wavelength limit, the 2D plasmon splits. However, further analysis of this phenomenon is beyond the scope of this paper.

Long living oscillations are not present for pristine graphene, as shown in Fig. 5. This is because the main contributions to the induced potential dynamics come from π and $\sigma + \pi$ plasmons which are very broad, i.e., well
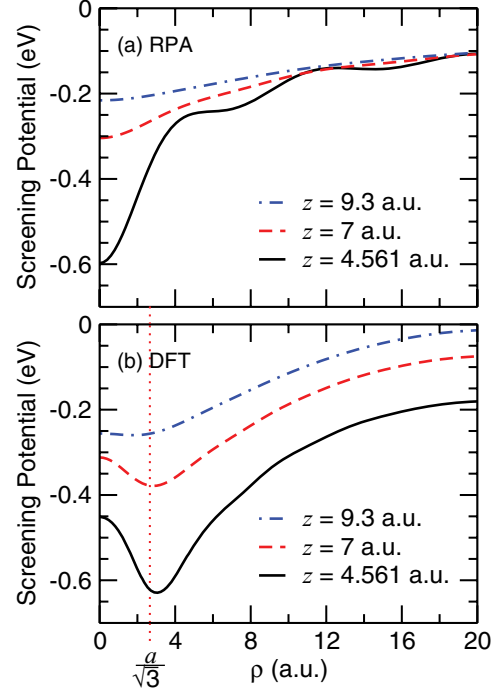

FIG. 6. (Color online) (a) RPA screening potential and (b) difference in DFT effective potential ΔV_{eff} in eV due to a C1s core hole at the origin vs radial coordinate ρ in a.u. for heights $z = 4.651$ a.u. (black solid line), $z = 7$ a.u. (red dashed line), and $z = 9.3$ a.u. (blue dash-dotted line) above the graphene layer. All energies are relative to the vacuum level E_{vac}.

damped. For this reason, the induced potential oscillates as an over-damped harmonic oscillator, exhibiting only one maximum for each plasmon.

B. Core-Hole Screening

We shall now investigate properties of the equilibrium core hole screening potential at large time scales ($t > 20$ fs) after the core hole is formed. Specifically, we consider the potential

$$V^{\text{scr}}(\rho,z) = V^{\text{ind}}(\rho,z,t \to \infty) + \frac{e^2}{\sqrt{\rho^2 + z^2}}, \qquad (31)$$

where the second term is the bare core hole potential contribution.

The RPA screening potential may be directly compared with the change in the DFT effective potential. The latter is the difference between the effective potential before and after removing one core C1s electron from the graphene layer. The supercell used in this calculation is a $9 \times 9 \times 1$ repetition of the primitive graphene unit cell. In this way interactions between periodic images of the core-hole may be neglected.

The difference between the DFT and RPA screening potentials can tell us about the importance of LFEs parallel to the graphene surface, which are neglected in the RPA calculations. On the other hand, the importance of long-range electron-electron correlations, which are excluded from the DFT calculations, will also be seen.

Figures 6(a) and 6(b) show the RPA screened core hole potential and the DFT effective potential difference,
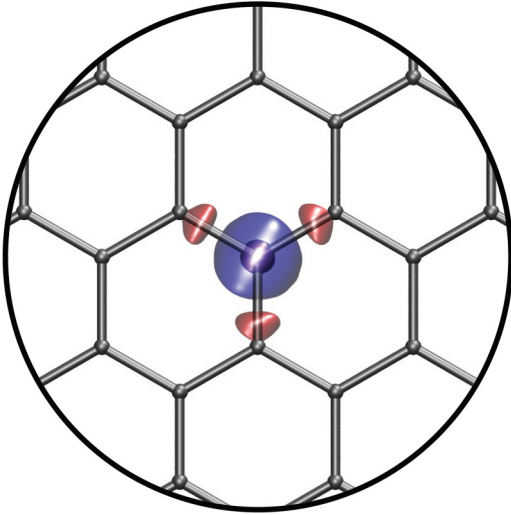
FIG. 7. (Color online) Schematic showing the change in DFT charge density $\Delta\rho$ due to a C1s core hole in a graphene layer. Isosurfaces of $\pm0.02e/\text{Å}^3$ in red and blue depict regions of positive and negative charge, respectively.

respectively, as functions of the radial coordinate ρ for three different heights z above the graphene monolayer. As expected, for the minimum perpendicular distance of $z = a \approx 4.651$ a.u., the difference between RPA and DFT results is the most significant. For the DFT result, we see oscillations from a local maximum at $\rho = 0$ to the minimum at about $\rho \approx 2.8$ a.u. This is because after the core hole is created, unfilled C3s states are pushed down in energy and the electrons from the surrounding nearest neighbor atoms start to fill it through their σ bonds.

From the induced density shown in Fig. 7 we see a surplus of electrons around the core hole and a deficit of electrons on the nearest-neighbor atoms. This clearly indicates charge transfer from the neighboring carbon atoms' σ bonds to the unoccupied 3s level on the atom with a 1s core hole. The enhanced screening in the core hole region, and reduction in the region of the surrounding atoms is positioned near $\rho = \frac{a}{\sqrt{3}} \approx 2.66$ a.u. We find this agrees quite well with the minimum in the DFT screening potential shown in Fig. 6(b).

This oscillation is not present in the RPA results because the effects of the crystal local field variations in the response function are averaged. In other words, the induced density is ρ dependent but isotropic and does not depend on the position of the core hole. On the other hand, for larger radial separations $\rho > 5$ a.u., Friedel oscillations occur as a consequence of long range electron-electron correlations. Such correlations are suppressed in the DFT calculations. The RPA induced potential behaves similarly to a 2D homogeneous electron gas.

As we would expect, for smaller radial separations $\rho < 5$ a.u. DFT results provide a more detailed description of the local variation of the screening potential compared to RPA. On the other hand, for larger radial separations $\rho > 5$ a.u., RPA provides a better description of the long range correlations.

Farther from the graphene monolayer, for $z \approx 7$ a.u. and $z \approx 9.3$ a.u. as shown in Fig. 6, qualitative differences between the RPA and DFT results decrease. This is because for $z > a$, as mentioned above, the microscopic crystal field variations become less important and Friedel oscillations do not occur.
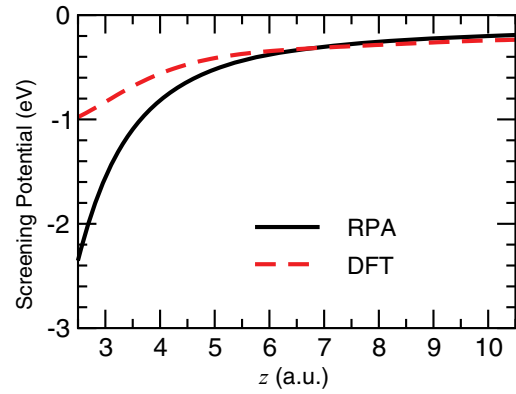

FIG. 8. (Color online) RPA screening potential (black solid line) and difference in DFT effective potential ΔV_{eff} (red dashed line) in eV due to a core hole at the origin vs height z in a.u. above the graphene layer for $\rho = 0$. All energies are relative to the vacuum level E_{vac}.

However, quantitative differences still remain. For example, the RPA potentials for all heights considered converge to one value, while the DFT potentials exhibit well separated long range tails. This disagreement is probably due to long range ($Q \to 0$) components of the induced density. These are present in RPA, and realign the induced potential at large ρ separations. However, there are no such $Q \to 0$ components in the DFT induced density.

For smaller ρ and larger z we find the DFT and RPA results shown near-quantitative agreement. This can be seen more clearly in Fig. 8, which shows DFT and RPA potentials as functions of the height z directly above the C1s core hole in the graphene monolayer at $\rho = 0$. Closer to the graphene surface, we see substantially stronger LDA screening. This is a consequence of the polarization of the dangling $2p_z$ orbitals, and the partially filled 3s orbital. For larger, $z > 6$. a.u., separations the DFT and RPA results begin to agree very well. This is because for large heights the microscopic details of the induced charge density around the core hole are not very important. Both methods, DFT which includes microscopic charge density variations, and RPA which does not include such variations, give the same result. As we have already mentioned, this is not the case far away from the core hole ($\rho > 5$ a.u.). This is because the DFT induced density decays exponentially while the RPA induced density has a long range character.

C. Ion Self Energy

Figure 9 shows a comparison between self energies obtained by using the full RPA self energy expression (21) and the image potential (IP) expression of Eq. (25), where the parameters Z and z_0 are obtained from Eqs. (24) and (26). For pristine graphene we obtain an effective image charge of $Z = 0.87$ and an effective image plane of $z_0 = 2.13$ a.u. Since the effective image charge is smaller than one, it seems that pristine graphene does not have an intrinsically metallic character, but rather is semimetallic. This is as expected, since pristine graphene has a zero band gap and only ultra soft $\pi \to \pi^*$ interband transitions can contribute to the conductivity. We also notice that the image potential continues to agree with the RPA potential down to short distances above the graphene monolayer of $z \approx 4$ a.u.
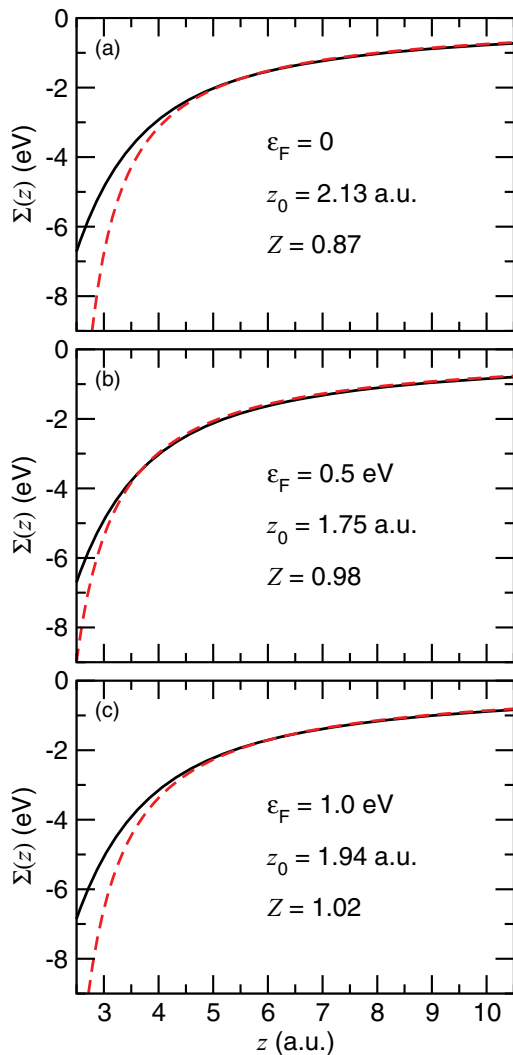
FIG. 9. (Color online) Self energy of the static point charge $\Sigma(z)$ in eV vs height z above a graphene layer, with doping of (a) $\varepsilon_F = 0$ eV, (b) $\varepsilon_F = 0.5$ eV, and (c) $\varepsilon_F = 1$ eV. RPA results (black solid line) are compared with the corresponding image potential (red dashed line), for z_0 and Z as provided.

The self energy of a charged particle near doped graphene is shown in Figs. 9(b) and 9(c) for $\varepsilon_F = 0.5$ eV and $\varepsilon_F = 1$ eV, respectively. For $\varepsilon_F = 0.5$ eV we obtain image potential parameters of $Z = 0.98$ and $z_0 = 1.75$ a.u. while for $\varepsilon_F = 1$ eV we obtain $Z = 1.02$ and $z_0 = 1.94$ a.u. Obviously doped graphene behaves as a metal because the effective image charge is $Z \approx 1$, corresponding to perfect DC conductivity. Also, we can see that the effective image plane increases as the density of effective charge carriers increases. All this agrees very well with the recent DFT ground state calculations of graphene in an external electrical field,[28] where the authors showed that the position of the centroid of the induced charge density is at $z_0 \approx 1.97$ a.u.

These results suggest that simple image theory is still applicable quite close ($z \geqslant 4$ a.u.) to a graphene monolayer. This means that for a proper description of the screening of an arbitrary static charge distribution placed at surprisingly small distances above a graphene monolayer, we only need to know
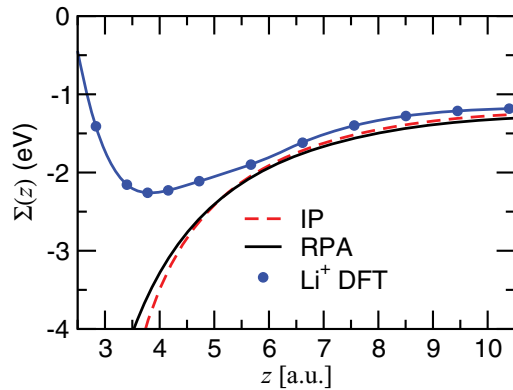

FIG. 10. (Color online) Self energy of the static point charge $\Sigma(z)$ in eV vs distance z between two pristine graphene layers at $z = 0$ and $z = L = 5a \approx 23.255$. RPA results (black solid line) are compared with the corresponding image potential (IP) (red dashed line), and the DFT self energy of a Li$^+$ ion (blue circles).

the static, long wavelength limit of the propagator $\widetilde{D}(Q, \omega)$. For a point charge this requires just two parameters, Z and z_0.

We now consider the self energy of a Li$^+$ ion placed close to a graphene monolayer as a function of the ion's height z above a graphene monolayer. As before, to perform the DFT calculation we need a periodic supercell consisting of graphene monolayers, with the Li$^+$ ion placed between the graphene layer and its periodically repeated image. For the graphene layer separation we take $L \approx 23.255$ a.u., as in the RPA calculation. In this case, the Li$^+$ ion polarizes both the graphene layer and its repeated image.

We use a pseudopotential for a Li$^+$ ion in vacuum, and perform a density functional calculation for Li$^+$ in a supercell consisting of $5 \times 5 \times 1$ repeated graphene primitive unit cells, with the charge of the system $Q = +1$ e. From a Bader analysis, we were able to verify that the Li atom stayed in the $+1$ state, so long as the atom was at least 1.5 Å away from the graphene surface. The self energy is then modeled using the total energy difference between two systems; one being the combined Li$^+$ and graphene with total charge $Q = +1$, and the other consisting of the neutral graphene surface and an isolated Li$^+$ ion.

To be able to compare these results with the previously described RPA self energy of the point charge, we have added the contribution from the polarization of the repeated image of the graphene layer placed at $z = L \approx 23.255$ a.u. In this procedure we have neglected the multiple polarization effects which we expect to be irrelevant at such interlayer separations.

Figure 10 shows the DFT calculated self energy of a Li$^+$ ion as a function of the height z above a graphene layer located at $z = 0$. Coulomb-like tails at larger separations suggests that there is a weak polarization of the net electron density in the ion. This means the electronic structure remains spherical and the ion behaves as a point charge.

This is also seen by comparing the DFT and RPA self energy of the point charge shown in Fig. 10. As we previously saw in Fig. 9(a), the RPA result again has an image potential behavior (25) where $Z \approx 0.87$ and $z_0 \approx 2.13$ a.u.. The DFT results also exhibit an image potential behavior, and there is little doubt that the Li$^+$ ion behaves as a point charge. However, closer

to the graphene monolayer the electronic orbitals of the Li^+ ion begin to overlap with the graphene electronic density. This results in the potential reaching a minimum at $z \approx 3.8$ a.u. before increasing nearer to the graphene monolayer.

To check the importance of long-range correlations, we also used the vdW-DF xc-functional[41] to calculate the Li^+ ion self energy. The vdW-DF calculations, not presented here, show that the Li^+ self energy at larger separations is reduced compared with the LDA result. This is because the vdW-DF functional includes long range contributions, which represent the coupling between charge density fluctuations in each of the interacting components. These interactions are not included in either the LDA-DFT case or in the RPA result, where we used point charges without any internal structure.

IV. CONCLUSIONS

In this paper we have used TDDFT-RPA to calculate the time dependence of the screened potential produced by the sudden creation of a C1s core hole in a graphene monolayer. We have shown that the characteristic features of the screened potential's dynamics are consequences of excitations of π, $\sigma + \pi$ and 2D plasmons in doped graphene. In particular, we have shown that short time scale features ($t < 2$ fs) of the induced potential are due to excitations of high energy π and $\sigma + \pi$ plasmons. On the other hand, the long time scale ($2 < t < 15$ fs) oscillations of the induced potential appear only when graphene is doped, and are due to excitations of low energy 2D plasmons.

We have compared the screened potential at equilibrium ($t \rightarrow \infty$) with the DFT effective potential. The latter is calculated in a supercell consisting of one C1s core hole in a much larger repeated graphene unit cell. We have shown that RPA and DFT equilibrium potentials are in qualitative agreement. This suggests that the more appropriate method of calculation of the screened potential is the less time-consuming RPA method, which is based on a primitive unit cell calculation.

We have calculated the self energy of a static point charge near a graphene monolayer and shown that it follows an image potential type behavior down to very short distances ($z \approx 4$ a.u.) above the graphene monolayer. The calculated image charge indicates a semimetallic character for pristine graphene and a metallic character for doped graphene. We have also compared the RPA and image potential results with a DFT calculation of the self energy for a Li^+ ion above a graphene monolayer. The three methods agreed near quantitatively down to short distances ($z \approx 5$ a.u.) above the graphene monolayer.

In summary, we have examined the efficiency, mechanism, and selectivity of excitations due to various types of plasmons in graphene. Our results have important implications not only for the description of the screening processes in core level spectroscopies, but also in the more general area of plasmonics. Specifically, the methods and results presented herein may be used to develop new plasmonic devices where a plasmon is excited by an arbitrary longitudinal probe, such as an external current, a charge transfer, or a quantum transition.

*vito@phy.br

[1] K. S. Novoselov, A. K. Geim, S. V. Morozov, D. Jiang, M. I. Katsnelson, I. V. Grigorieva, S. V. Dubonos, and A. A. Firsov, Nature (London) **438**, 197 (2005).

[2] Y. Zhang, Y. W. Tan, H. L. Stormer, and P. Kim, Nature (London) **438**, 201 (2005).

[3] K. S. Novoselov, A. K. Geim, S. V. Morozov, D. Jiang, Y. Zhang, S. V. Dubonos, I. V. Grigorieva, and A. A. Firsov, Science **306**, 666 (2004).

[4] K. S. Novoselov, D. Jiang, F. Schedin, T. J. Booth, V. V. Khotkevich, S. V. Morozov, and A. K. Geim, Proc. Natl. Acad. Sci. USA **102**, 10451 (2005).

[5] A. K. Geim and K. S. Novoselov, Nat. Mater. **6**, 183 (2007).

[6] I. Pletikosić, M. Kralj, P. Pervan, R. Brako, J. Coraux, A. T. N'Diaye, C. Busse, and T. Michely, Phys. Rev. Lett. **102**, 056808 (2009).

[7] M. O. Goerbig, Rev. Mod. Phys. **83**, 1193 (2011).

[8] S. Das Sarma, Shaffique Adam, E. H. Hwang, and Enrico Rossi, Rev. Mod. Phys. **83**, 407 (2011).

[9] A. H. Castro Neto, F. Guinea, N. M. R. Peres, K. S. Novoselov, and A. K. Geim, Rev. Mod. Phys. **81**, 109 (2009).

[10] A. H. Castro Neto and K. Novoselov, Rep. Prog. Phys. **74**, 082501 (2011).

[11] K. S. Novoselov, Rev. Mod. Phys. **83**, 837 (2011).

[12] Andre K. Geim, Rev. Mod. Phys. **83**, 851 (2011).

[13] Sangita Bose, Vyacheslav M. Silkin, Robin Ohmann, Ivan Brihuega, Lucia Vitali, Christian H. Michaelis, Pierre Mallet, Jean Yves Veuillen, M. Alexander Schneider, Evgueni V. Chulkov, Pedro M. Echenique, and Klaus Kern, New J. Phys. **12**, 023028 (2010).

[14] Y. Zhang, Tsung-Ta Tang, C. Girit, Z. Hao, Michael C. Martin, A. Zettl, Michael F. Crommie, and Y. Ron Shen Feng Wang, Nature (London) **459**, 820 (2009).

[15] Farhan Rana, Nat. Nanotechnol. **6**, 611 (2011).

[16] F. Bonaccorso, Z. Sun, T. Hasan, and A. C. Ferrari, Nat. Photon. **4**, 611 (2010).

[17] M. Jablan, H. Buljan, and M. Soljačić, Phys. Rev. B **80**, 245435 (2009).

[18] Frank H. L. Koppens, Darrick E. Chang, and F. Javier García de Abajo, Nano Lett. **11**, 3370 (2011).

[19] Sung Won Hwang, Dong Hee Shin, Chang Oh Kim, Seung Hui Hong, Min Choul Kim, Jungkil Kim, Keun Yong Lim, Sung Kim, Suk-Ho Choi, Kwang Jun Ahn, Gunn Kim, Sung Hyun Sim, and Byung Hee Hong, Phys. Rev. Lett. **105**, 127403 (2010).

[20] B. N. J. Persson and H. Ueba, J. Phys.: Condens. Matter **22**, 462201 (2010).

[21] Yu. V. Bludov, M. I. Vasilevskiy, and N. M. R. Peres, Europhys. Lett. **92**, 68001 (2010).

[22] E. H. Hwang and S. Das Sarma, Phys. Rev. B **75**, 205418 (2007).

[23] Yi Gao and Zhe Yuan, Solid State Commun. **151**, 1009 (2011).

[24] V. Borka Jovanović, I. Radović, D. Borka, and Z. L. Mišković, Phys. Rev. B **84**, 155416 (2011).

[25] C. Tegenkamp, H. Pfnur, T. Langer, J. Baringhaus, and H. W. Schumacher, J. Phys.: Condens. Matter **23**, 012001 (2011).

[26] T. Eberlein, U. Bangert, R. R. Nair, R. Jones, M. Gass, A. L. Bleloch, K. S. Novoselov, A. Geim, and P. R. Briddon, Phys. Rev. B **77**, 233406 (2008).

[27] Jiong Lu, Kian Ping Loh, Han Huang, Wei Chen, and Andrew T. S. Wee, Phys. Rev. B **80**, 113410 (2009).

[28] V. M. Silkin, J. Zhao, F. Guinea, E. V. Chulkov, P. M. Echenique, and H. Petek, Phys. Rev. B **80**, 121408 (2009).

[29] Paolo Giannozzi, Stefano Baroni, Nicola Bonini, Matteo Calandra, Roberto Car, Carlo Cavazzoni, Davide Ceresoli, Guido L. Chiarotti, Matteo Cococcioni, Ismaila Dabo, Andrea Dal Corso, Stefano de Gironcoli, Stefano Fabris, Guido Fratesi, Ralph Gebauer, Uwe Gerstmann, Christos Gougoussis, Anton Kokalj, Michele Lazzeri, Layla Martin-Samos, Nicola Marzari, Francesco Mauri, Riccardo Mazzarello, Stefano Paolini, Alfredo Pasquarello, Lorenzo Paulatto, Carlo Sbraccia, Sandro Scandolo, Gabriele Sclauzero, Ari P. Seitsonen, Alexander Smogunov, Paolo Umari, and Renata M. Wentzcovitch, J. Phys.: Condens. Matter **21**, 395502 (2009).

[30] J. J. Mortensen, L. B. Hansen, and K. W. Jacobsen, Phys. Rev. B **71**, 035109 (2005).

[31] J. Enkovaara, C. Rostgaard, J. J. Mortensen, J. Chen, M. Dułak, L. Ferrighi, J. Gavnholt, C. Glinsvad, V. Haikola, H. A. Hansen, H. H. Kristoffersen, M. Kuisma, A. H. Larsen, L. Lehtovaara, M. Ljungberg, O. Lopez-Acevedo, P. G. Moses, J. Ojanen, T. Olsen, V. Petzold, N. A. Romero, J. Stausholm-Møller, M. Strange, G. A. Tritsaris, M. Vanin, M. Walter, B. Hammer, H. Häkkinen, G. K. H. Madsen, R. M. Nieminen, J. K. Nørskov, M. Puska, T. T. Rantala, J. Schiøtz, K. S. Thygesen, and K. W. Jacobsen, J. Phys.: Condens. Matter **22**, 253202 (2010).

[32] J. P. Perdew and Alex Zunger, Phys. Rev. B **23**, 5048 (1981).

[33] W. Kohn and L. J. Sham, Phys. Rev. **140**, A1133 (1965).

[34] Hendrik J. Monkhorst and James D. Pack, Phys. Rev. B **13**, 5188 (1976).

[35] N. Troullier and José Luriaas Martins, Phys. Rev. B **43**, 1993 (1991).

[36] V. Despoja, D. J. Mowbray, and V. M. Silkin, Phys. Rev. B **84**, 104514 (2011).

[37] D. J. Mowbray, V. Despoja, P. Ayala, T. Pichler, and A. Rubio (unpublished).

[38] C. Kramberger, R. Hambach, C. Giorgetti, M. H. Rümmeli, M. Knupfer, J. Fink, B. Büchner, Lucia Reining, E. Einarsson, S. Maruyama, F. Sottile, K. Hannewald, V. Olevano, A. G. Marinopoulos, and T. Pichler, Phys. Rev. Lett. **100**, 196803 (2008).

[39] C. Kramberger, F. Roth, R. Schuster, R. Kraus, M. Knupfer, E. Einarsson, S. Maruyama, D. J. Mowbray, A. Rubio, and T. Pichler, Phys. Rev. B **85**, 085424 (2012).

[40] V. Despoja, M. Šunjić, and L. Marušić, Phys. Rev. B **77**, 035424 (2008).

[41] M. Dion, H. Rydberg, E. Schröder, D. C. Langreth, and B. I. Lundqvist, Phys. Rev. Lett. **92**, 246401 (2004).